

Enhancement of confocal microscopy images using Mueller-matrix polarimetry

J.M. BUENO*, C.J. COOKSON†, M.L. KISILAK†‡
& M.C.W. CAMPBELL†‡§

*Laboratorio de Óptica, Centro de Investigación en Óptica y Nanofísica, Universidad de Murcia,
Campus de Espinardo, 30100 Murcia, Spain

†Department of Physics and Astronomy, University of Waterloo, Waterloo, ON, Canada

‡School of Optometry, University of Waterloo, Waterloo, ON, Canada

§Guelph-Waterloo Physics Institute, Waterloo, ON, Canada

Key words. Confocal microscopy, image improvement, polarimetry.

Summary

A simplified procedure based on Mueller-matrix polarimetry has recently been reported as a method of retinal image improvement in a confocal ophthalmoscope [J. M. Bueno *et al.*, J. Opt. Soc. Am. A 24, 1337 (2007)]. Here, we have applied the technique to imaging static samples providing well-defined reflection properties. The method uses a generator of polarization states in the illumination pathway of a confocal scanning laser system. From the calculated four elements of the Mueller matrix of any sample and instrument combination, the best images defined by different metrics were constructed. For samples with specular, diffuse and mixed reflections, the best-constructed images showed an enhancement in both objective and subjective image quality compared to the original images and those obtained from frame averaging. This technique could improve microscopic imaging in many diverse fields, particularly in biomedical imaging.

Introduction

Minsky's patented confocal microscope (Minsky, 1957) was the precursor of a large variety of experimental set-ups, devices and applications. The instrument has been improved in different ways, including the use of new illumination sources and scanning systems, as well as faster and more accurate recording methods. Although objects can be imaged with greater contrast and clarity than is possible with conventional, non-confocal microscopes, an increase in both lateral and depth resolutions has been the overriding aim in the development of this type of microscopy. In particular, the

contributions to resolution of the wavelength of the light, the numerical aperture of the objective lens, and pinhole and detector size have been studied in detail (Wilson & Sheppard, 1984; White *et al.*, 1987; Wilson, 1990; Pawley, 1991; Chen *et al.*, 1995; Wilson, *et al.*, 1998).

Confocal microscopy has been used in the analysis of different samples ranging from biological specimens (living cells, tissues) to inorganic surfaces (Beesley *et al.*, 1995; Chen *et al.*, 1995; Ribes *et al.*, 1995; Dailey *et al.*, 1999; Li *et al.*, 2000). Recently, adaptive optics has been reported to improve contrast and axial resolution in confocal microscopy (Booth *et al.*, 2002). Moreover, the confocal effect has also been incorporated into ophthalmoscopes (Webb *et al.*, 1987), which are instruments used for viewing the *in vivo* ocular fundus, where the ocular optics replace the microscope objective.

The incorporation of polarization into microscopy imaging techniques has enhanced the quality of the images by reducing stray light and increasing their contrast (Dixon *et al.*, 1991; Chen *et al.*, 1995; Oldenbourg & Mei, 1995). A polarizing microscope is an instrument that uses a polarizer and an analyzer (both mounted on a rotating stage) to look at materials under polarized light. Although polarizing microscopes have been used mainly for detailed tissue analysis for diagnostic pathology (Wolman, 1975; Yaroslavsky *et al.*, 2005), studies on non-biological specimens have also been reported (Robinson & Gleeson, 1993; Wasiak & Sajkiewicz, 1995; Kawata & Inami, 1998).

The authors of this paper have reported the use of complete Mueller-matrix polarimetry in a confocal scanning laser system (in both ophthalmoscope and microscope modes) to reduce noise and improve contrast in retinal images containing blood vessels and in samples giving specular reflections (Bueno & Campbell, 2002). However, since just 4 out of 16 elements of the Mueller matrix are used to construct the image intensity, this technique has recently been simplified

Correspondence to: J.M. Bueno. Tel: +34-8688 88 335; fax: +34-8688 83 528;
e-mail: bueno@um.es

by reducing the number of recorded images from 16 to 4 (Campbell *et al.*, 2005; Bueno *et al.*, 2007). Moreover, in this simpler method, the analyzer unit in the recording pathway and the calibration procedure are not required. Images of the optic nerve head have been improved using this simplified method as quantified by three different image quality metrics (Hunter *et al.*, 2007). Here we test this polarimetric technique in a confocal scanning laser microscope (CSLM) with static samples, which reflect light differently. We also discuss which image quality metric incorporated into the technique yields the most improvement in contrast and visibility of features in the image.

Materials and Methods

Experimental system

Figure 1 shows a schematic diagram of the CSLM used for the present study. The light source is a He-Ne laser (633 nm). The beam is expanded and collimated before entering the polarization state generator, composed of a fixed vertical linear polarizer (P) and a rotating quarter-wave plate (QWP). Beam size is controlled by aperture AP1. A polygon mirror and a galvanometer act as a raster scanning unit allowing horizontal and vertical scans, respectively.

Light reflected from the sample passes back through the scanning unit, so that the beam is stationary when incident on the beam splitter (BS) and reaches the recording arm, which is composed of a collector lens (CL), a confocal pinhole (AP2) and a detector (photo-multiplier tube). A series of four videos of the sample corresponding to independent incoming polarization states are recorded. These polarization states are achieved in the generator unit by rotating the fast axis of QWP as described elsewhere (Bueno *et al.*, 2003). Apertures AP1 is conjugated

with the entrance pupil of the microscope objective and AP2 is conjugate with the sample imaged.

The inset of Fig. 1 corresponds to a removable analyzer unit which has a symmetric configuration with respect to the generator unit. When including this unit, the complete Mueller matrix can be obtained (Bueno & Campbell, 2002). Alternatively, it was also used in a subset of experiments to compute changes in the degree of polarization of the light (computed from the emergent Stokes vector as described below) returning from the samples under study.

Since the CSLM contains optical elements that could be polarization-dependent, the intensity reaching the detector and the image quality might be influenced by them. Just four elements of the Mueller matrix (experimental system + sample) have influence on the final recorded image. These have been calculated from four views of the object through the generator and used to improve image quality as explained in the following section.

Theory

From the images recorded for four different incoming polarization states of light, background images are subtracted, the elements of the first row of the Mueller matrix of the combination of the sample under study and the CSLM ($M_0 = m_{0k}$ ($k = 0, 1, 2, 3$)) are computed as broadly explained in a subsequent paper (Bueno *et al.*, 2007). Briefly, for each independent polarization state produced in the generator, $S_G^{(i)}$ ($i = 1, 2, 3, 4$), the recorded image $I_F^{(i)}$ is a result of:

$$\begin{aligned}
 I_F &= \begin{pmatrix} I_F^{(1)} \\ I_F^{(2)} \\ I_F^{(3)} \\ I_F^{(4)} \end{pmatrix}^T \\
 &= \begin{pmatrix} m_{00} \\ m_{01} \\ m_{02} \\ m_{03} \end{pmatrix}^T \cdot \begin{pmatrix} S_{0G}^{(1)} & S_{0G}^{(2)} & S_{0G}^{(3)} & S_{0G}^{(4)} \\ S_{1G}^{(1)} & S_{1G}^{(2)} & S_{1G}^{(3)} & S_{1G}^{(4)} \\ S_{2G}^{(1)} & S_{2G}^{(2)} & S_{2G}^{(3)} & S_{2G}^{(4)} \\ S_{3G}^{(1)} & S_{3G}^{(2)} & S_{3G}^{(3)} & S_{3G}^{(4)} \end{pmatrix} \\
 &= M_0 \cdot M_G,
 \end{aligned} \tag{1}$$

where M_G is a 4×4 matrix containing the four Stokes vectors $S_G^{(i)}$. Since I_F is a different vector for each pixel in the image, the elements of the M_0 are spatially varying over the object. Finally, M_0 is obtained by means of:

$$M_0 = I_F \cdot (M_G)^{-1}. \tag{2}$$

At this point, our objective was to improve the images obtained by using the elements of M_0 and their differing properties over the object. For this aim, we computed the images $I^{(OUT)}$ corresponding to a set of incident Stokes vectors covering the Poincaré sphere in increments of 5 deg in azimuth (χ) and

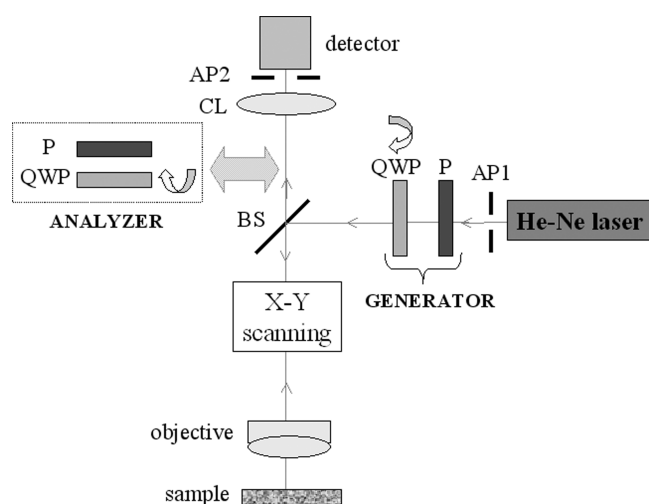


Fig. 1. Simplified schematic diagram of the experimental set-up. P, vertical linear polarizers; QWP, rotating quarter-wave plates; BS, beam splitter; CL, collector lens; AP1 and AP2, apertures.

ellipticity (φ), as shown in Eq. (3):

$$I^{(OUT)} = M_0 \cdot S_{IN}(\chi, \varphi) \quad (3)$$

where an image is generated by performing the calculation for a given Stokes vector at each image pixel. We have previously shown that the quality of CSLO images depends on the incident Stokes vector (Bueno & Campbell, 2002; Campbell *et al.*, 2005; Bueno *et al.*, 2007). The image $I^{(OUT)}$ with best quality (in terms of a defined metric) was chosen from images computed for all Stokes vectors and the corresponding Stokes vector was recorded. This method allows images to be constructed for polarization states, which cannot be produced in an experimental system. In this work, we will use three different metrics to quantify image quality: signal-to-noise ratio (SNR), entropy and acutance. Definitions of the image quality metrics can be found elsewhere (Goodman, 1984; Hunter *et al.* 2007). All image processing was done in MatLab (The MathWorks, Inc.). We also assessed the resulting contrast and visibility of features in the images.

If the analyzer unit is included in the system, then for each incident polarization state, the Stokes vector associated with the light reaching the analyzer after reflection from the sample, S_{OUT} , can be computed as:

$$S_{OUT} = \begin{pmatrix} S_0 \\ S_1 \\ S_2 \\ S_3 \end{pmatrix} = (M_{PSA})^{-1} \begin{pmatrix} I_{-45} \\ I_0 \\ I_{30} \\ I_{60} \end{pmatrix}, \quad (4)$$

where I_j ($j = -45, 0, 30, 60$) are the images registered for each independent orientation of the QWP of the analyzer unit (keeping the generator fixed) and M_{PSA} is the auxiliary 4×4 matrix defined in Bueno *et al.* (2003).

The vector S_{OUT} contains information on the polarization properties of the sample and the instrument in combination. In particular, the degree of polarization (DOP) of the light emerging from the sample can be directly computed as (Chipman, 1995):

$$DOP = \frac{(S_1^2 + S_2^2 + S_3^2)^{1/2}}{S_0} \quad (0 \leq DOP \leq 1). \quad (5)$$

Alternatively, depolarization is defined as 1-DOP, which ranges from 0 (totally polarized light) to 1 (depolarized or natural light).

Samples, confocal pinholes, field scans and imaging

The main goal of this work was to test our method and its ability to enhance features of interest on static samples, which reflect light differently. The samples were placed on a three-axis micrometric stage. A grey scale picture printed on a matte paper and two different USAF resolution charts, providing primarily diffuse and primarily specular reflections respectively (see Results), were imaged. Images at differing depths were also taken of a computer microchip, primarily

specular and of a commercial tissue sample mounted on a glass slide with cover slip (human cerebrum sample). The last reflected a mixture of diffuse and specular light. Imaging was repeated on the computer microchip.

The instrument configuration used varied with the target. The grey scale picture and lower resolution USAF target (consisting of gold bars on glass) were imaged in a $\sim 10^\circ$ field between the final two telescope lenses, using a confocal pinhole larger than ideal. For these two targets, Mueller-matrix calculations were performed with single frames.

For the next three samples, the beam was focused onto by means of a Mitutoyo Apo100 200 mm focal length microscope objective with a 0.7 numerical aperture (NA). Images of the microchip and high resolution USAF target (consisting of clear glass bars on a chromium background) were taken using the 3° field with a small confocal pinhole. The USAF targets were tilted to remove interference between the reflections from the two glass surfaces, which would invalidate a Stokes vector analysis. A white sheet was mounted behind the second glass surface. The human cerebrum sample was taken with a 6° field and a moderate pinhole to allow for a brighter image. For the tissue sample, pairs of images were added together to double the signal. This led to no further saturation of the pixels in the image. In terms of intensity, this is analogous to doubling the exposure time while taking images with a CCD camera. For these three samples, eight images corresponding to each input polarization state were averaged together prior to calculation of the top row of the Mueller matrix.

Since depolarization is associated with the presence of scattering and diffusion (Chipman, 1995; Bueno *et al.*, 2004), this property can be used to test the nature of the reflection of the samples under study. The higher the depolarization (lower DOP), the higher the scattering produced.

To determine the DOP of the light returning from the sample, the analyzer unit was included in the recording pathway (see Fig. 1) and the generator unit was set to produce circularly polarized light. Four video segments of the sample were recorded, each corresponding to an independent orientation of the QWP of the analyzer. For the diffuse paper target and the gold USAF target, single-frame images were used with Eqs (4) and (5), to compute S_{OUT} and DOP. For the other three targets, eight-frame averages corresponding to an independent orientation of the QWP of the analyzer were used to compute S_{OUT} and DOP.

Results

Spatially resolved degree of polarization

As an example, Fig. 2 shows the spatially resolved Stokes vector, S_{OUT} in Eq. (4) (at each image pixel) corresponding to a grey scale image printed on paper. The incident light was circularly polarized. In S_1 , S_2 and S_3 , the pixel values are both positive and negative, corresponding to differing polarizations.

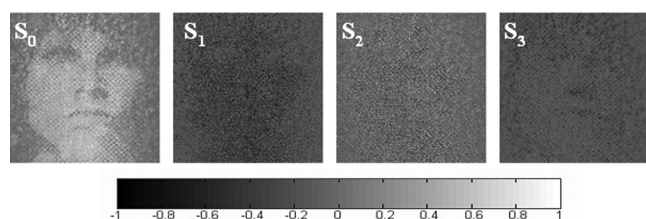


Fig. 2. Spatially resolved elements of the Stokes vector in a transposed position corresponding to a picture printed on matte paper (diffuse reflection). The grey level code is shown at the bottom.

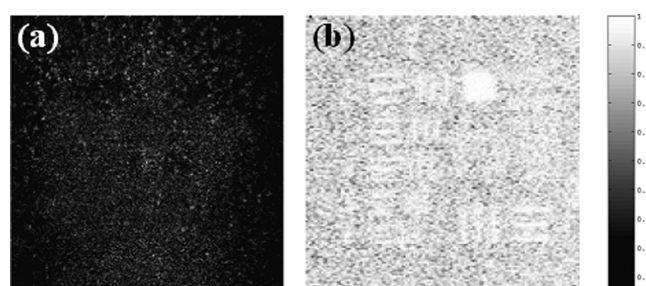


Fig. 3. Maps for the DOP of the picture printed on paper (a) and a USAF resolution chart (sputtered gold on glass) (b). Images subtend 10 and 4.4 mm (356 and 140 pixels, respectively).

This sample is presumed to diffusely reflect. From these elements, the map corresponding to the DOP was also calculated (Fig. 3(a)). The average DOP (and standard deviation) across the whole image was 0.23 ± 0.02 . This high depolarization produced by this sample confirms its diffusely reflecting nature.

More specular reflections were studied by means of USAF resolution charts and a microcomputer chip. Figure 3(b) depicts the results of the DOP determination for the gold on glass USAF target. For the USAF target, the averaged DOP (and standard deviation) was 0.99 for an area of the gold bar and 0.89 for an area of the glass. These values indicate that the light reflected from the target remains highly polarized and that the amount of scattered light recorded is low. The chromium USAF target was also highly polarized with a DOP of 0.93 on the clear glass and 0.99 on the chromium. The difference between the DOP of the glass and metallic areas likely arose from a small amount of scattered light from the white paper behind the targets. The computer microchip was also highly specular with a DOP of 0.91 on the top of the target and 0.94 at the bottom. The tissue sample showed a DOP of 0.7 at all three focal planes, suggesting that the reflection of the sample dominated was a mixture of diffuse and specular reflections.

Improved image quality through frame averaging

It is well known that scanning laser images can easily be improved by frame averaging, which reduces noise due to laser

Table 1. Values of SNR, entropy and acutance as a result of frame averaging for two different samples.

# Frames	SNR		Entropy		Acutance	
	1	8	1	8	1	8
Diffuse	2.02	2.23	6449	7881	91	43
Specular	2.64	2.88	5472	5941	274	116

speckle and from the detector. Averaged images are improved due to a reduction in the effect of additive random noise. The changes in different image quality metrics in relation to the number of images in the average has been presented for confocal scanning laser ophthalmoscope images (Hunter *et al.*, 2007). For comparison, the improvement in image quality given by averaging the same number of frames as used in the polarimetry calculation was calculated.

Table 1 shows the corresponding values for the three image quality metrics used here for the diffuse and one of the specular targets. For all samples, a noticeable subjective improvement and an objective improvement in SNR and entropy after frame averaging is observed. On the other hand, acutance is higher in the unaveraged images and its reduction in averaged images appears to be associated with a decrease in noise. These results agree with those reported for retinal images (Hunter *et al.*, 2007).

Improved image quality using four elements of the Mueller matrix

In this sub-section, we will quantify the improvement in confocal images with differing reflection properties using just four elements of the Mueller matrix (M_{00} , M_{01} , M_{02} and M_{03}), using the procedure described above. We will also investigate which image quality metric in the calculation gives the best improvement in contrast and visibility of features.

For the image on paper (diffuse sample), the upper row of Fig. 4 presents the four raw one-frame polarimetric images (elements of vector I_F in Eq. (1)). For each of the three metrics, the highest value for the raw images corresponded to circularly polarized light ($I_F^{(1)}$).

The spatially resolved elements of the first row of the Mueller matrix (vector M_0) were computed using Eqs (1) and (2) and are also shown. In spite of being a depolarizing sample, the values of M_{01} are nonzero and spatially varying across the image. There is less information in elements M_{02} and M_{03} , which represent the interaction of the sample with $\pm 45^\circ$ linear and circularly polarized light, respectively.

From the elements of the Mueller matrix, images $I^{(OUT)}$ of Eq. (3) were calculated and the images with the maximum (and minimum) values of SNR, entropy and acutance were chosen (Fig. 5). The metric values corresponding to the four original images were always between the highest and the lowest values

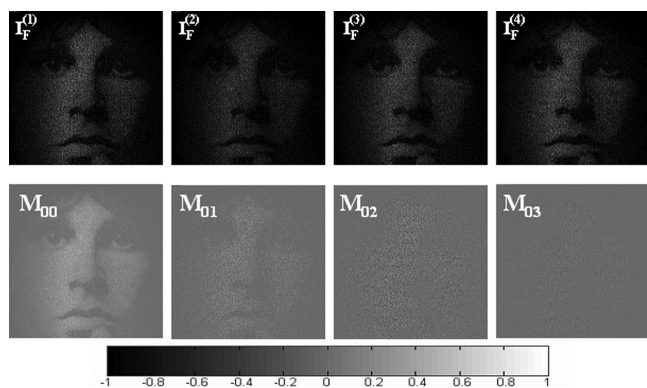


Fig. 4. Original raw images (upper panels) corresponding to the four polarization states in the generator unit for a diffuse sample (image on paper). Elements of the first row of the spatially resolved Mueller matrix (bottom row). The grey level code is shown at the bottom. Each image subtends 2 cm and 256 pixels.

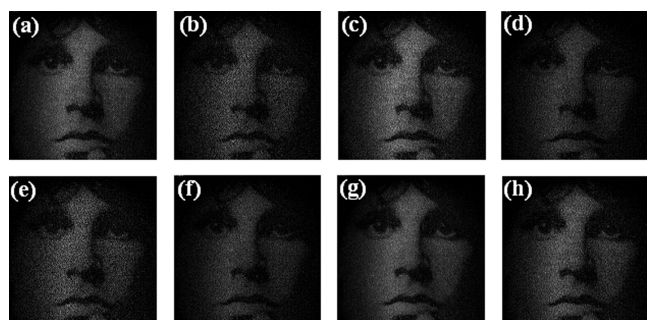


Fig. 5. Results of image improvement corresponding to the diffuse paper sample in Fig. 4: images with maximum (a) and minimum (b) SNR; maximum (c) and minimum (d) entropy; maximum (e) and minimum (f) acutance; for incident non-polarized light (g) and the averaged of eight raw frames for linear incident light (h).

obtained with the procedure described here. For comparison, the computed image for incident non-polarized light as well as the averaged image for eight original frames are also included.

The improvement in the images obtained using the polarization method over the other images was noticeable subjectively. Higher contrast in particular areas is seen in the constructed images with maximum SNR, entropy and acutance compared to the initial images. For this sample, constructed images with a maximum value for these metrics provide better image quality than any of the original ones. Furthermore, values of SNR, entropy and acutance corresponding to the average of eight original frames taken with linear polarization were always below the maximum values obtained with our procedure.

As a quantitative example and for better comparisons, entropy and acutance values are depicted in Fig. 6. The plot depicts the values corresponding to the original image with highest entropy and acutance as well as those for the constructed images with maximum and minimum values for

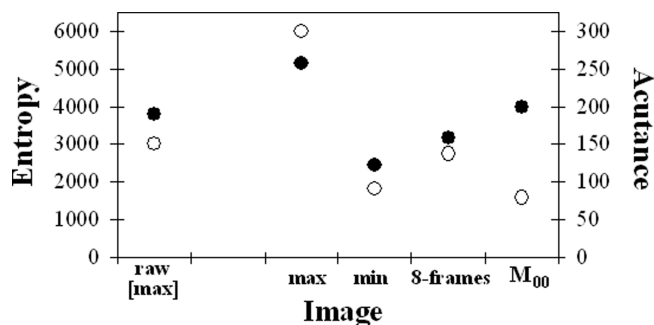


Fig. 6. Values of entropy (black dots) and acutance (white dots) for the diffuse paper sample. Labels on the horizontal axis corresponds to the original image with maximum entropy and acutance ('raw[max]'), constructed images with maximum and minimum entropy and acutance ('max' and 'min'), eight-frame average image ('8-frames') and the image for non-polarized light (M_{00}).

those metrics. Moreover, we have also included the data for the eight-frame average images (linearly polarized incident light) and for the image (M_{00}) corresponding to non-polarized light. Although the improvement is different for each metric, the best-constructed polarization image has a higher metric value than that corresponding to the eight-frame averaged image, the depolarized image or the initial images. Of the metrics used to construct the images, in this case, maximum entropy provided the image with a combination of the best contrast and visibility of fine detail.

In the following, we present the results for the USAF target with gold bars. Figure 7 shows the elements of the Mueller matrix. All elements of M_0 have values different from zero, primarily indicating an interaction with linear and circular polarized light. From the elements of M_0 , the images providing the maximum and minimum values for SNR, entropy and acutance were constructed. Results are presented in Fig. 8. As in the case of the diffuse image, the best-constructed polarization image has a higher metric value than that corresponding to the eight-frame averaged image taken in linearly polarized light or the initial images. This also happened with (or for) the depolarized image, except for SNR where values for the best-reconstructed image and the M_{00} image

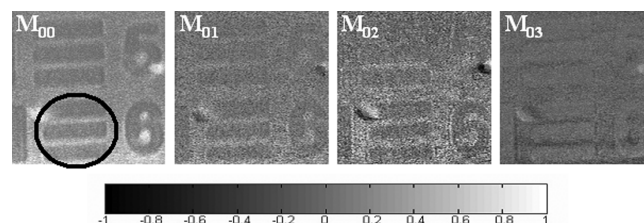


Fig. 7. Elements of the first row of the Mueller matrix (M_0) of the USAF chart with gold bars. Details in the encircled zone correspond to an area with a resolution of 28.5 lines/mm. Images are approximately 105 microns and are 186 pixels square.

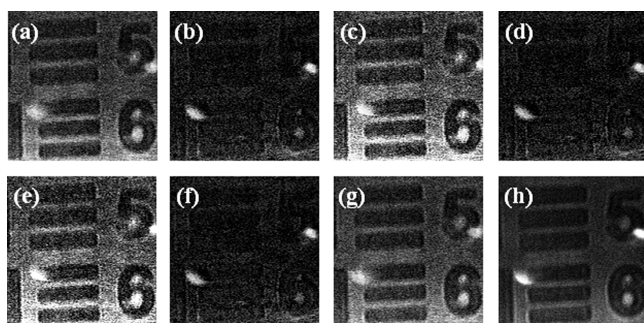


Fig. 8. Constructed images for the gold USAF target computed from the Mueller-matrix elements in Fig. 7. The figure shows constructed images with maximum (a) and minimum (b) SNR, maximum (c) and minimum (d) entropy, maximum (e) and minimum (f) acutance, for incident non-polarized light (g) and the average of eight raw frames for linear incident light (h).

were similar. Of the metrics used to construct the images, in this case, maximum entropy provided the image with a combination of the best contrast and visibility of fine detail. The entropy improvement with respect to the best original image was 24%.

Figure 9 shows results for the chromium USAF target with higher resolution. Again, the best-constructed polarization images have higher metric values for entropy than that corresponding to the 32-frame averaged image (23%), but similar values to the depolarized image or the best initial image. Again, the noise in initial averaged images may be the cause

of higher acutance values than in the constructed images. Although the 32-frame average of the initial image in linearly polarized light had a higher SNR than the constructed images with maximum SNR or maximum entropy, the constructed images appear subjectively better than the 32-frame average. The average image shows lower contrast of features than the best-constructed images shown (Fig. 9). The best initial image was for incident circularly polarized light.

Figure 10 shows results for another specular reflecting target of potential interest to microscopists: a computer microchip imaged at two different depths. Here the constructed polarization image with maximum entropy has a higher metric value than that corresponding to the 32-frame averaged image, the depolarized image or the initial images. The improvements (approximately 4%) are lower for the focus at the top of the number than when the focus is at the bottom of the numbers (21%). SNR in the frame-averaged image is higher than in the polarimetry images, although the subjective quality, contrast and visibility of fine features are lower in this image (Fig. 10). Acutance follows the same pattern as for the chromium USAF target. The images with maximum entropy and maximum SNR are subjectively similar. The best initial image quantified by maximum entropy was for incident circular polarization while the best initial image quantified by SNR was for elliptically polarized light.

Images of the chip were taken on two different occasions. The best initial image was always at the same polarization, circular for entropy and elliptical for SNR. Image subtraction

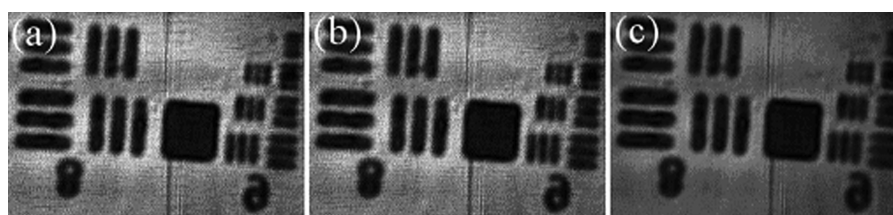


Fig. 9. Images of a USAF target with glass bars surrounded by chromium. The central line is an artefact of background subtraction. The highest resolution shown is 645 lines/mm, giving a resolution approaching 1.5 microns. Shown are the constructed images with maximum entropy (a), maximum SNR (b) and an average of 32 frames taken with linearly polarized light (c). Image size is 44.7 microns and 260 pixels across.

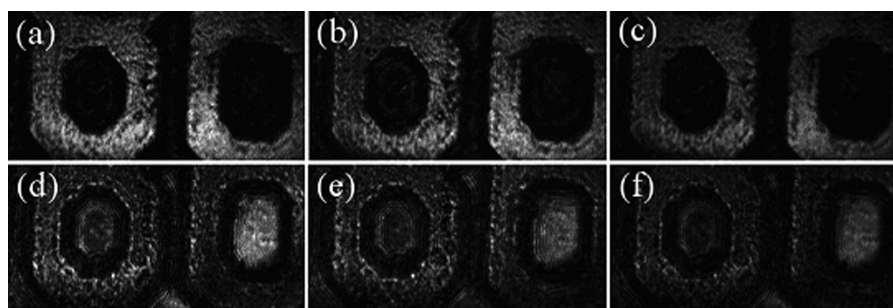


Fig. 10. Images of sections of numbers on a specularly reflecting computer chip imaged in two planes shown above and below, 10 microns apart in depth. The images on the left (a and d) are those constructed with maximum entropy while the ones in the centre (b and e) are those constructed with maximum SNR. The images on the right are the average of 32 frames taken with linearly polarized light. Image size is 51.6 microns and 300 pixels across.

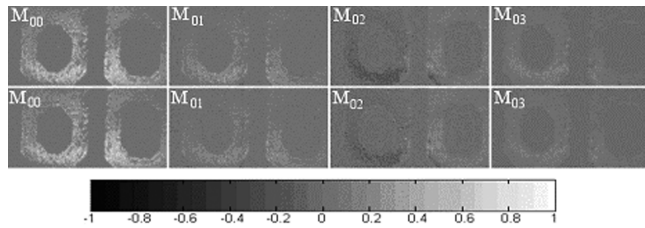


Fig. 11. Elements of the first row of the Mueller matrix (M_{00}) calculated from images of the computer chip on two different occasions.

shows broad similarity of the polarimetry images with differences likely arising due to rapid changes in image brightness with small changes of focus in depth. The Mueller matrix was very similar in the two runs (Fig. 11). The maximum entropy image showed slightly different improvements in the second run (6% on top and 10% on bottom). For the repeated measurement shown (Fig. 11), the maximum entropy value differed by 3.1% and the Stokes vectors for maximum entropy differed by $< 10^\circ$ on the Poincaré sphere.

Figure 12 shows images of a biological target, a section of cerebrum. Here again the best-constructed polarization images for entropy and SNR have higher metric values than that corresponding to the 32-frame averaged image or the initial images. In one case, the values of SNR for the constructed image were lower than for the depolarized image

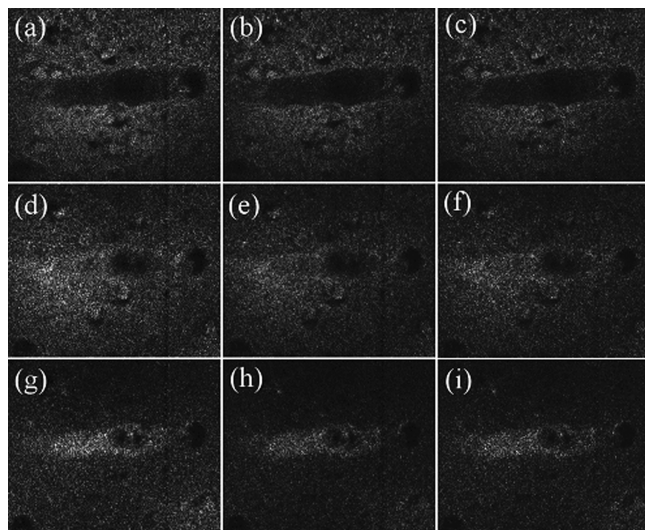


Fig. 12. Images of optical sections through a tissue section of cerebrum, imaged in three planes, shown vertically and spaced 8 microns apart in depth. The section is through a cerebral sulcus from the anterior (top) to posterior (bottom) part of the sample. The vertical lines are artefacts of background subtraction. Images were constructed with, on the left, maximum entropy (a, d and g) and, in the centre, maximum SNR (b, c and h). Shown on the right (c, f and h) are images that are 32-frame averages taken with linearly polarized light. Image size is 137.6 microns and 400 pixels across.

(4%). Images with maximum entropy had higher contrast and visibility of features than any of the other metric conditions. The polarimetry method gave an average of 21% improvement in entropy compared to other images. The best initial image, quantified by SNR varied in its incident polarization while for entropy the best initial image was again for incident circularly polarized light.

Features on both the microchip and the tissue sample were resolved in depth (Figs 10 and 12) with each optical slice showing improved image quality in the computed best polarimetric images (using SNR and entropy) compared to the four experimentally recorded images.

The Stokes vectors, which correspond to the constructed images with the best image quality, depend on both the metric and the sample (reflection characteristics and the size of the details imaged). In general, the incident polarization, which produces the best initial quality as well as the polarization corresponding to the best-constructed image, is elliptical. Sometimes, the polarization state corresponding to the best-constructed image is close to circular polarization resulting in little difference between this image and the initially acquired image.

Discussion

We have presented a technique for increasing the quality of the images taken with a CSLM using polarized light. Our previous method (Bueno and Campbell, 2002) has been modified to avoid a calibration procedure and to reduce image recording and processing times. With our simplified method, from four recorded images (each for an independent polarization state produced in the generator unit), the elements of the first row of the Mueller matrix of the CSLM + sample were computed. From these elements, the images corresponding to the maximum and the minimum values of three global image quality metrics were constructed by mathematically changing the incoming polarization state. We chose to maximize and minimize each metric since the maximum value for a particular metric does not guarantee the best image (Bueno *et al.*, 2007). Any other numerical descriptor (metric) of image quality is applicable here. The chosen metrics can also be optimized across different areas of interest in the image in order to enhance them separately (Bueno *et al.*, 2007; Hunter *et al.*, 2007). For the specular and diffusely reflecting targets investigated here as well as the tissue sample with a partially specular reflection, the metric maximum entropy consistently produced images, which had the best contrast and visibility of features in the image. Acutance did not vary in a systematic way with frame averaging and polarimetry. However, the best metric may depend on the sample (Bueno *et al.*, 2007). In the case of small, somewhat ordered features, the image with maximum acutance may be subjectively better than any of the original images.

We were interested in applying our method to static samples providing well-defined specular and diffuse reflections associated with different amounts of depolarization as well as to targets well suited to microscopy, which could be optically sectioned. Results showed that the DOP ranged from 0.23 for a depolarizing sample to 0.99 for the most specular reflection. These values confirm the different nature of the samples we analysed: almost non-depolarizing (specular) and highly depolarizing (diffusing) and two samples of user interest (a microchip with specular reflections and a tissue sample with mixed reflections). At least one metric produced superior constructed images regardless of the nature of the reflection. Smaller improvements occurred when the ideal polarization was close to circular, one of the initial illumination polarizations. In general, the position on the Poincaré sphere of the Stokes vector which gave the best image was elliptical and differed from the illumination polarizations and also varied between samples.

The best-constructed images using this method had both objectively improved image quality (as quantified by metrics) and better contrast and visibility of features compared with the original images. This resulted in more structural details and small features being observed, which were less discernible in the original images. In images with a lower DOP, the values for Mueller-matrix element M_{01} and M_{02} still vary across the image. In spite of their low values, considering all possible incident Stokes vectors linearly combines the Mueller-matrix elements to give an image of better quality. This indicates that the spatial distributions of different Mueller-matrix elements differ. Thus, the method described here is useful even for targets, which depolarize most of the incident light or interact little with polarized light and show relatively small values of diattenuation. This is in contrast to previous polarization imaging methods, which rely on either an optical isotropy or on preservation of polarization (Demos *et al.*, 1996). Unlike some previous polarization imaging methods, the one described here considers incident light of all polarization states rather than solely linear polarization (Tyo, 2000; Burns *et al.*, 2003). Circularly polarized light often gives the best initial and/or constructed images.

Image improvement by means of frame averaging is well known. However, one of the most interesting results presented here is that the best-constructed image was better than the frame average image for linear incident light for both types of reflection. This is important because the best-constructed polarization image is derived from multiple measured images. That is, our procedure is able to improve the image quality more than in frame averaging alone.

Our technique also allows comparison with the image corresponding to non-polarized incident light (element M_{00}), although the real illumination corresponds to a polarized source. In each case for the most useful metric, maximum entropy, and in a large majority of cases for SNR, the best-constructed image was also better than that corresponding to

depolarized light. This reinforces that, although depolarized images might show an improvement in quality compared with images with a particular input polarization (Demos *et al.*, 2000; Burns *et al.*, 2003), our method is likely to show further improvement.

Many objects appear optically isotropic but show various kinds of contrast when viewed through two-crossed linear polarizers. This fact has been used in polarization microscopes in both reflection and transmission modes to enhance imaging (Kocsis *et al.*, 1998). Nowadays, this technique is included in the most expensive microscopes and is used to explore the spatial orientation patterns of individual macromolecules, to determine localization and directional orientation of collagen fibres, for topographic analysis and for imaging through turbid media among others (Speer & Dahners, 1979; Gleyzes *et al.*, 1997; Kocsis *et al.*, 1998; Forkey *et al.*, 2005; Yaroslavsky *et al.*, 2005). It has been reported that polarizing microscopes improve the detection of tiny structures in different tissues (Wolman, 1975; Sun *et al.*, 2001; Oron *et al.*, 2003; Wang *et al.*, 2003; Yaroslavsky *et al.*, 2005). In multi-photon microscopy, polarization also helps to enhance the visibility of features and sub-surface structures (Higgins *et al.*, 1996; Sun *et al.*, 2005). Polarization has also been included in scanning near-field optical microscopy. These instruments perform polarization contrast imaging by rotating the input linear polarization over all possible directions. This offers additional information over working with one fixed polarization (Rowe *et al.*, 1995). Our method has the advantage of considering circularly and elliptically polarized light in addition to all linear polarizations.

During the last decade, polarization has been used to improve other imaging techniques. In general, polarization imaging has been reported to improve contrast, reduce noise and provide useful information about scenes (not available with polarization-blind imaging). In particular, polarization-difference imaging (PDI, i.e. the difference between images registered with parallel and crossed linear polarizers) was used for imaging through scattering media (Mickols & Maestre, 1988; Tyo *et al.*, 1996; Tyo, 2000; Gan & Gu, 2002). More recently, polarization gating methods have improved images through turbid media in a transmission-mode microscope (Jiao *et al.*, 2000). It has recently been reported that polarimetric parameters extracted from the Mueller matrix of samples in transmission improve the detection of tiny structures not seen in original images (Campbell *et al.*, 2007).

On the other hand, polarization-sensitive optical coherence tomography is emerging as a very attractive branch of imaging science (Jiao *et al.*, 2000; Hitzengerger *et al.*, 2001; de Boer, 2002). This technique can reveal important information about fibrous structures in biological tissue, which is not available in conventional optical coherence tomography.

The present method constructs images corresponding to a large set of Stokes vectors with linear, circular and elliptical polarization (not just linear incident polarization used in

established polarization microscopy). Many of these might be difficult to generate in an experimental set-up. In addition, only a polarization generator is required, improving the amount of light incident onto the detector compared with a set-up with crossed polarizers or a generator/analyzer set-up for full Mueller-matrix analysis. Our set-up is particularly advantageous when measuring samples that are light sensitive or samples with low reflectivity. The amount of light incident on the generator (and the sample) can also be adjusted. The images taken can also be analysed in a spatially resolved manner. That is, the constructed images that highlight features in different regions of the image may be different even though they are calculated from the same initial images.

The present measurements have been centred on static, artificial samples with large and small DOPs as well as on samples of intrinsic interest, which could be optically sectioned. The microscope has been used in reflection mode, but slight changes would allow the method to be applied to samples in transmission mode. In particular, the use of the present method in biological samples is of great interest, especially in those samples for which either the light level reflected is low, leading to high noise or the contrast is low and needs to be increased. The fact that most biological tissues, tendons and bones have measurable polarization properties may make this a successful tool with broad application in biomedical fields.

The implementation of this technique in confocal ophthalmoscopes has been reported to increase the resolution and contrast of retinal images (Bueno *et al.*, 2007). However, the incorporation into other retinal imaging systems such as fundus cameras and optical coherence tomography devices may potentially aid in ocular disease diagnosis. Moreover, this technique could be a low-cost alternative or an addition to adaptive optics in providing improved contrast and potentially improved resolution (Song *et al.*, 2008).

Conclusion

We have compared the performance of novel polarization-based and frame-averaged confocal microscopy imaging in samples providing different types of reflections. Results show that optimized images can be constructed using just images with four original polarization states. These constructed images have better quality than the images obtained from frame averaging the images initially acquired with linearly polarized light. In the method, for a wide range of reflection types (specular, diffuse and mixed reflections), maximizing the metric entropy consistently produced images with an increased value of this objective metric as well as increased contrast and subjective visibility of features.

Acknowledgements

This work was supported by NSERC (Canada), Photonics Research Ontario and grant FIS2007-64765 from the Ministerio de Educación y Ciencia (Spain). The authors thank James McPherson for comments on the manuscript.

References

- Beesley, K.M., Damaskinos, S. & Dixon, A.E. (1995) Fingerprint imaging with a confocal scanning laser MACROscope®. *J. Forensic Sci.* **40**, 10–17.
- Booth, M.J., Neil, M.A.A., Juskaitis, R. & Wilson, T. (2002) Adaptive aberration correction in a confocal microscope. *PNAS* **99**, 5788–5792.
- Bueno J.M. & Campbell, M.C.W. (2002) Confocal scanning laser ophthalmoscopy improvement by using Mueller-matrix polarimetry. *Opt. Lett.* **27**, 830–832.
- Bueno, J. M., Berrio, E. & Artal, P. (2003) Aberro-polariscope for the human eye. *Opt. Lett.* **28**, 1209–1211.
- Bueno, J.M., Berrio, E., Ozolinsh, M. & Artal, P. (2004) Degree of polarization as an objective method of estimating scattering. *J. Opt. Soc. Am. A* **21**, 1316–1321.
- Bueno, J. M., Hunter, J.J., Cookson, C.J., Kisilak, M.L., & Campbell, M.C.W. (2007) Improved scanning laser fundus imaging using polarimetry. *J. Opt. Soc. Am. A* **24**, 1337–1348.
- Burns, S.A., Elsner, A.E., Mellem-Kairala, M.B. & Simmons, R.B. (2003) Improved contrast of subretinal structures using polarization analysis. *Invest. Ophthalmol. Vis. Sci.* **44**, 4061–4068.
- Campbell, M.C.W., Bueno, J.M., Cookson, C.J., Liang, Q., Kisilak, M.L. & Hunter, J.J. (2005) Enhanced confocal microscopy and ophthalmoscopy with polarization imaging. *Proc. SPIE* **5969**, 611–616.
- Campbell, M.C.W., Cookson, C.J., Bueno, J.M., Seaman A.N. & Kisilak, M.L. (2007) Confocal polarimetry measurements of tissue infected with malaria, 2007 OSA Technical Digest: *Frontiers in Optics*, Optical Society of America, 2007, pp. FThK1.
- Chen, H., Swedlow, J.R., Grote, M., Sedat, J.W. & Agard, D.A. (1995) The collection, processing, and display of digital three-dimensional images of biological specimens. *Handbook of Biological Confocal Microscopy* (ed. by J. B. Pawley), pp. 197–210. Plenum Press, New York.
- Chipman, R. A. (1995) Polarimetry. *Handbook of Optics*, vol. 2, 2nd edn, Chap. 22. McGraw-Hill, New York.
- Dailey, M., Marrs, G., Satz, J. & Waite, M. (1999) Exploring biological structure and function with confocal microscopy. *Biol. Bull.* **197**, 115–122.
- de Boer, J.F. (2002) Review of polarization sensitive optical coherence tomography and stokes vector determination. *J. Biomed. Opt.* **7**, 359–371.
- Demos, S.G., Savage, H., Heerdt, A.S., Schantz, S. & Alfano, R.R. (1996) Temporal polarization preservation in human breast tissue – a method for optical imaging. *Proc. SPIE* **2965**, 40–43.
- Demos, S.G., Radousky, H.B. & Alfano, R.R. (2000) Deep subsurface imaging in tissues using spectral and polarization filtering. *Opt. Express* **7**, 23–28.
- Dixon, A.E., Damaskinos, S. & Atkinson, M.R. (1991) A scanning confocal microscope for transmission and reflection imaging. *Nature* **351**, 551–553.

- Forkey, J.N., Quinlan, M.E. & Goldman, Y.E. (2005) Measurement of single macromolecule orientation by total internal reflection fluorescence polarization microscopy. *Biophys. J.* **89**, 1261–1271.
- Gan, X. & Gu, M. (2002) Image reconstruction through turbid media under a transmission-mode microscope. *J. Biomed. Opt.* **7**, 372–377.
- Gleyzes, P., Boccara, A.C. & Saint-Jalmes, H. (1997) Multichannel Nomarskimicroscope with polarization modulation: performance and applications. *Opt. Lett.* **22**, 1529–1531.
- Goodman, J. W. (1984) Statistical properties of laser speckle patterns. *Laser Speckle and Related Phenomena*, vol. 9 of *Topics in Applied Physics*, 2nd edn (ed. by J. C. Dainty) pp. 9–75. Springer-Verlag, Berlin.
- Higgins, D.A., Vanden Bout, D.A., Kerimo, J. & Barbara, P.F. (1996) Polarization-modulation near-field scanning optical microscopy of mesostructured materials. *J. Phys. Chem.* **100**, 13794–13803.
- Hitzenberger, C.K., Götzinger, E., Sticker, M. & Fercher, A.F. (2001) Measurement and imaging of birefringence and optic axis orientation by phase resolved polarization sensitive optical coherence tomography. *Opt. Express* **9**, 780–790.
- Hunter, J.J., Cookson, C.J., Kisilak, M.L., Bueno, J.M. & Campbell, M.C.W. (2007) Characterizing image quality in a scanning laser ophthalmoscope with differing pinholes and induced scattered light. *J. Opt. Soc. Am. A* **24**, 1284–1295.
- Jiao, S., Gang, Y. & Wang, L.V. (2000) Depth-resolved two-dimensional Stokes vectors of backscattered light and Mueller matrices of biological tissue measured with optical coherence tomography. *Appl. Opt.* **39**, 6318–6324.
- Kawata, Y. & Inami, W. (1998) Confocal microscope for three-dimensional polarization analysis. *Jpn. J. Appl. Phys.* **37**, 6648–6650.
- Kocsis, K., Hyttinen, M., Helminen, H.J., Aydelotte, M.B. & Modis, L. (1998) Combination of digital image analysis and polarization microscopy: theoretical considerations and experimental data. *Microsc. Res. Tech.* **43**, 511–517.
- Li, J., Jester, J.V., Cavanagh, H.D., Black, T.D. & Petroll, W.M. (2000) On-line 3-dimensional confocal imaging in vivo. *Invest. Ophthalmol. Vis. Sci.* **41**, 2945–2953.
- Mickols, W. & Maestre, M.F. (1988) Scanning differential polarization microscope: its use to image linear and circular differential. *Rev. Sci. Instr.* **59**, 867–872.
- Minsky, M. (1957) U. S. Patent #3013467.
- Oldenbourg R. & Mei, G. (1995) New polarized light microscope with precision universal compensator. *J. Microsc.* **180**, 140–147.
- Oron, D., Tal, E. & Silberberg, Y. (2003) Depth-resolved multiphoton polarization microscopy by third-harmonic generation. *Opt. Lett.* **28**, 2315–2317.
- Pawley, J.B. (1991) Fundamental and practical limits in confocal microscopy. *Scanning* **13**, 184–198.
- Ribes, A.C., Damaskinos, S., Dixon, A.E. Ellis, K.A., Duttagupta, S.P. & Fauchet, P.M. (1995) Confocal imaging of porous silicon with a scanning laser MACROscope[®]/microscope. *Prog. Surf. Sci.* **50**, 295–304.
- Robinson, W. K. & Gleeson, H.F. (1993) A polarizing microscope for high-pressure studies of liquid crystals. *Meas. Sci. Technol.* **4**, 1238–1243.
- Rowe, M.P., Pugh, E.N. Jr., Tyo, J.S. & Engheta, N. (1995) Polarization-difference imaging: a biological inspired technique for observation through scattering media. *Opt. Lett.* **20**, 608–610.
- Song, H., Zhao, Y., Qi, X., Chui, Y. T. & Burns, S. A. (2008) Stokes vector analysis of adaptive optics images of the retina. *Opt. Lett.* **33**, 137–139.
- Speer, D.P. & Dahners, L. (1979) The collagenous architecture of articular cartilage. Correlation of scanning electron microscopy and polarized light microscopy observations. *Clin. Orthop. Relat. Res.* **139**, 267–275.
- Sun, C., Wang, C., Yang, C.C., Kiang, Y., Lu, C., Hsu, I. & Lin, C. (2001) Polarization-dependent characteristics and polarization gating in time-resolved optical imaging of skeletal muscle tissues. *IEEE J. Quant. Elect.* **1**, 924–930.
- Sun, Y., Su, J., Lo, W., Lin, S., Jee, S. & Dong, C. (2005) Applications of multiphoton polarization and generalized polarization microscopy in elucidating transdermal delivery pathways. *Proc. SPIE* **5686**, 59–66.
- Tyo, J.S. (2000) Enhancement of the point-spread function for imaging in scattering media by use of polarization -difference imaging. *J. Opt. Soc. Am. A* **17**, 1–10.
- Tyo, J.S., Rowe, M.P., Pugh, E.N. Jr. & Engheta, N. (1996) Target detection in optically scattering media by polarization-difference imaging. *Appl. Opt.* **35**, 1855–1870.
- Wang, W. B., Ali, J.H., Alfano, R.R., Vitenson, J.H. & Lombardo, J.M. (2003) Spectral polarization imaging of human rectum-membrane-prostate tissues. *IEEE J. Quant. Elect.* **9**, 288–293.
- Wasiak, A. & Sajkiewicz, P. (1995) Polarizing microscope for studies of the effects of an electric field on crystallization of polymers. *Opt. Eng.* **34**, 3393–3397.
- Webb, R.H., Hughes, G.W. & Delori, F.C. (1987) Confocal scanning laser ophthalmoscope. *Appl. Opt.* **26**, 1492–1499.
- White, J.G., Amos, W.B. & Fordham, M. (1987) An evaluation of confocal versus conventional imaging of biological structures by fluorescence light microscopy. *J. Cell Biol.* **105**, 41–48.
- Wilson, T. (1990) *Confocal Microscopy*. Academic Press, London.
- Wilson T. & Sheppard, C. (1984) *Theory and Practice of Scanning Optical Microscopy*. Academic Press, London.
- Wilson, T., Török, P. & Higdson, P.D. (1998) The effect of detector size on the signal-to-noise ratio in confocal polarized light microscopy. *J. Microsc.* **189**, 12–14.
- Wolman, M. (1975) Polarized light microscopy as a tool of diagnostic pathology. A review. *J. Histchem. Cytochem.* **23**, 21–50.
- Yaroslavsky, A.N., Barbosa, J., Neel, V., DiMarzio, C. & Anderson, R.R. (2005) Combining multispectral polarized light imaging and confocal microscopy for localization of nonmelanoma skin cancer. *J. Biom. Opt.* **10**, 014011.